

Face-centered tetragonal (FCT) Fe and Co alloys of Pt as catalysts for the oxygen reduction reaction (ORR): A DFT study

Cite as: J. Chem. Phys. **150**, 041704 (2019); <https://doi.org/10.1063/1.5049674>

Submitted: 24 July 2018 • Accepted: 03 October 2018 • Published Online: 08 November 2018

Shubham Sharma, Cheng Zeng and  Andrew A. Peterson

COLLECTIONS

Paper published as part of the special topic on [Interfacial Electrochemistry and Photo\(electro\)catalysis](#)



[View Online](#)



[Export Citation](#)



[CrossMark](#)

ARTICLES YOU MAY BE INTERESTED IN

[A consistent and accurate ab initio parametrization of density functional dispersion correction \(DFT-D\) for the 94 elements H-Pu](#)

The Journal of Chemical Physics **132**, 154104 (2010); <https://doi.org/10.1063/1.3382344>

[Beneficial compressive strain for oxygen reduction reaction on Pt \(111\) surface](#)

The Journal of Chemical Physics **141**, 124713 (2014); <https://doi.org/10.1063/1.4896604>

[Modification of the surface electronic and chemical properties of Pt\(111\) by subsurface 3d transition metals](#)

The Journal of Chemical Physics **120**, 10240 (2004); <https://doi.org/10.1063/1.1737365>

[Learn More](#)

The Journal
of Chemical Physics **Special Topics** Open for Submissions

Face-centered tetragonal (FCT) Fe and Co alloys of Pt as catalysts for the oxygen reduction reaction (ORR): A DFT study

Cite as: J. Chem. Phys. 150, 041704 (2019); doi: 10.1063/1.5049674

Submitted: 24 July 2018 • Accepted: 3 October 2018 •

Published Online: 8 November 2018



View Online



Export Citation



CrossMark

Shubham Sharma, Cheng Zeng, and Andrew A. Peterson^{a)} 

AFFILIATIONS

School of Engineering, Brown University, Providence, Rhode Island 02912, USA

^{a)} Electronic mail: andrew.peterson@brown.edu

ABSTRACT

Proton exchange membrane fuel cells (PEMFCs) are promising candidates for alternate energy conversion devices owing to their various advantages including high efficiency, reliability, and environmental friendliness. The performance of PEMFCs is fundamentally limited by the sluggish kinetics of the oxygen reduction reaction (ORR) at the cathode. Various studies have addressed myriads of Pt-based alloys as potential catalysts for ORR. However, most of these studies only focus on the cubic-structured Pt-based alloys which require further improvements especially in terms of stability and required loading. In this work, we perform first-principle density functional theory calculations to explore Fe and Co alloys of Pt in a different face centered tetragonal (L_{10}) geometry as potential catalysts for ORR. The work focuses on understanding the reaction mechanism of ORR by both dissociative and associative mechanisms on L_{10} -FePt/Pt(111) and L_{10} -CoPt/Pt(111) surfaces. The binding pattern of each reaction intermediate is studied along with the complete reaction free energy landscape as a function of Pt overlayers. The L_{10} -FePt/Pt(111) and L_{10} -CoPt/Pt(111) surfaces show higher calculated surface activity for ORR as compared to the native fcc Pt(111) surface. The decrease in the required overpotential (η) for the alloys with respect to the unstrained Pt(111) surface is found to be in the range (0.04 V–0.25 V) assuming the dissociative mechanism and (0.02 V–0.10 V) assuming the associative mechanism, where the variation depends on the thickness of Pt overlayers. We further correlate the binding behavior of the reaction intermediates to the applied biaxial strain on the Pt(111) surface with the help of a mechanical eigenforce model. The eigenforce model gives a (semi-) quantitative prediction of the binding energies of the ORR intermediates under applied biaxial strain. The numerical values of the limiting potential (U_L) obtained from the eigenforce model are found to be very close to ones obtained from electronic structure calculations (less than 0.1 V difference). The eigenforce model is further used to predict the ideal equi-biaxial strain range required on Pt(111) surfaces for optimum ORR activity.

Published under license by AIP Publishing. <https://doi.org/10.1063/1.5049674>

I. INTRODUCTION

One of the most attractive applications of proton exchange membrane fuel cells (PEMFCs) is their use in the automobile industry to drive high-power electric vehicles.¹ Representing a convergence of the trend of the electrification of the drivetrain with the concept of the “hydrogen economy,” a fuel cell efficiently exploits the chemical energy stored in hydrogen gas to generate electricity which can be used to drive electric cars.^{2–4} PEMFCs have seen recent commercial demonstration in the automobile industry, but their

large-scale production still faces several challenges. Many of these challenges are related to the relatively slow kinetics of the oxygen reduction reaction (ORR) at the cathode;^{5–7} this necessitates the use of a high overpotential and directly lowers the efficiency of the fuel cell. Pt is the best elemental electrocatalyst for ORR, and in addition to its high cost it suffers from relatively high cathodic overpotential requirements of around 0.4 V at a current density of 1 mA cm^{-2} . Pt being scarce in quantity makes it even more challenging to develop principles for designing scalable catalysts that exhibit high surface activity as well as low Pt loading at the

same time. Alloying Pt with a less expensive first-row transition metal like Co, Ni, or Fe is one such common strategy that has been explored for the efficient design of ORR catalysts.^{8–10} In particular, the core/shell structured Pt alloys with a thin Pt shell and a metal(M)-Pt core provides an interesting and promising direction for ORR catalysts that can exhibit higher per-site activity in addition to reducing the use of Pt both via dilution and with a high surface-to-mass ratio. The ORR activity of core/shell-structured MPt alloy nanoparticles are usually considered in terms of strain and ligand effects.^{11–18} The strain effect is due to the lattice mismatch of the shell with the core, while the ligand effect arises due to the electronic interaction between the shell and the core constituents.

Basic catalyst theory suggests that an optimal catalyst should follow the Sabatier principle: binding the reactant intermediates neither too weakly nor too strongly.⁷ That is, a good ORR catalyst should be reactive enough to activate the O₂ bond and at the same time noble enough to release intermediates like HO* from the surface to form H₂O. (Here, * represents an adsorption site.) Additionally, too strong binding of reaction intermediates is believed to block most of the active sites on the catalyst surface, hindering the ability to break the O–O bond. However, too weak binding of O* makes breaking the O–O bond energetically unfavorable. Pt is known to bind O* and HO* relatively strongly, which may be responsible for the slow kinetics of ORR. Theoretical studies have proposed that a good ORR catalyst should bind ORR intermediates like O* around 0.0–0.4 eV weaker or HO* around 0.0–0.2 eV weaker as compared to Pt(111).^{6,19,20} The effect of strain and ligand effects on the binding strength of a reaction intermediate can be associated with the shift in the surface d-band center as described by the conventional d-band center model.^{12,21} There have been various studies using electronic structure theory which focused on understanding the effect of strain and/or ligand on ORR intermediates due to the change in the surface d-band center.^{7,11–18,22,23} It has been established that compressive biaxial strain and/or ligand effects can lead to the down-shift of Pt's surface d-band center, leading towards weaker binding of the ORR reaction intermediates.²⁴ For example, Stamenkovic *et al.*¹⁴ have reported 10-fold increase in ORR activity for Pt₃Ni(111) resulting from the combination of both strain and ligand effects arising from a special arrangement of the surface which consisted of a Pt-enriched outermost layer and a Ni-enriched subsurface. In particular, it is a conceived notion that compressive strain in the Pt shell layer is beneficial for enhancing the ORR activity of many MPt catalysts.

Investigations on some MPt alloys, especially in the form of core-shell nanostructures, revealed the strain effect to be dominant in tuning the ORR activity due to the acid leaching of the solute element.^{15,25–27} A detailed investigation on Pt₅M (M = lanthanide or alkaline earth metal) electrocatalysts reported improved ORR activity by a factor of three to six over Pt as a result of strain effects introduced on the Pt shell by

lanthanide contraction. Pt₅Tb and Pt₅Gd showed the highest activity among this set, which corresponds to a lateral compressive strain of 5.5% and 4.7%, respectively.²⁷ In order to study just the effect of ligands on ORR activity, Duan and Wang¹⁰ performed density functional theory (DFT) calculations on Pt/M(111) (M = Ni, Co, Fe) alloy catalysts. The modeled surfaces were assumed to have the same lattice constant as unstrained fcc Pt, modified with a transition metal enriched subsurface. Their theoretical study reported that the presence of subsurface transition metals like Ni, Co, and Fe can lead to multi-fold enhancement in the ORR catalytic activity as a result of a pure ligand effect. Deconvolution of the ligand and strain effect is considered as a difficult task for many MPt alloy systems; most of the theoretical studies discussed above focus on understanding only one of the effects. Incorporating theoretical studies to understand the predominance of either strain or ligand effects based on different surface/subsurface compositions and alloying elements is required to better understand and improve the design of ORR catalysts. The use of MPt alloys to enhance the ORR activity with the help of the strain and/or ligand effect has shown an interesting direction for designing better ORR catalysts. However, the stabilization of secondary metals (M) like Fe, Co, and Ni in MPt alloys still remains a challenging task owing to the extremely corrosive conditions at the fuel cell cathode, and many of these metals can damage the fuel cell's membrane if they leach from the catalyst over the lifetime of the cell. Most of the studied cubic structured MPt alloys, despite showing improved ORR activity, are not known to efficiently stabilize the secondary metal (M) under the acidic ORR conditions. On the other hand, a recent study on tetragonal L1₀-structured FePt has shown efficient Fe stabilization against acid leaching along with enhanced ORR activity as compared to cubic structured Pt₃Fe.²⁸

Motivated by these experimental L1₀ structures, in the current study, we use density functional theory (DFT) to perform a detailed investigation on core-shell structured L1₀-MPt/Pt (M = Fe, Co) alloys for enhancing the ORR activity as a function of Pt shell thickness. The work focuses on studying the strain and ligand effects on binding strengths of the ORR intermediates and the ORR surface activity. We will show that DFT calculations predict enhanced ORR activity for both L1₀-FePt/Pt(111) and L1₀-CoPt/Pt(111) surfaces as compared to the unstrained Pt(111) surface. We attribute the enhancement in ORR activity to the dominating strain effect on the Pt(111) surface in the case of ~3 or more Pt overlayers. The ligand effect becomes more dominant for 1–2 Pt overlayers which may further tune the ORR activity. We will show that we can use an intuitive eigenstress model²⁹ to explain the trends in binding energy with pure applied compressive strain. The eigenstress model has shown that the interaction potential energy can be described by the coupling between the adsorbate-induced surface stress with the external strain. An intuitive “eigenforce” model is proposed based on the eigenstress model which aims towards providing a (semi-) quantitative prediction of the binding energy change due to a pure strain effect. The eigenforce model shows similar trends

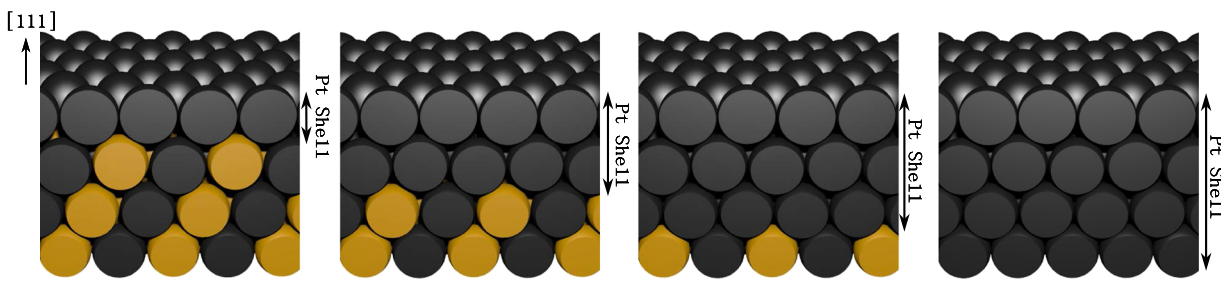


FIG. 1. Schematic showing a side cut view of $L1_0$ -MPt/Pt_n slabs (M = Fe, Co) with increasing Pt overayers from left to right. Here, n denotes the number of Pt overayers.

for the effect of applied compressive strain on adsorbate binding strengths as seen through the conventional d-band center model and is also able to approximately predict the experimentally observed ideal equi-biaxial strain required on the Pt(111) surface for near-optimum ORR activity.

II. COMPUTATIONAL METHODS

Electronic structure calculations were performed in density functional theory (DFT) using a Grid-Based Projector-Augmented Wave (GPAW)^{30,31} method with atomistic manipulations handled in the Atomic Simulation Environment (ASE).³² We used a plane wave basis set along with the revised Perdew-Burke-Ernzerhof (RPBE) exchange-correlation functional of Hammer, Hansen, and Nørskov.³³ The surfaces were modeled using a 3×4 unit cell with four atomic layers and 15 Å vacuum in the z-direction. For all the surface calculations, we fixed the bottom layer of the slab, while the top three layers and the adsorbates were allowed to relax. The optimized RPBE bulk lattice constants were used for modeling the Pt(111), L1₀-FePt/Pt_n(111), and L1₀-CoPt/Pt_n(111) surfaces. Here, n represents the number of Pt overayers ($1 \leq n \leq 4$). The optimized bulk lattice constants for Pt, L1₀-FePt, and L1₀-CoPt were ($a = 3.99$ Å), ($a = 3.90$ Å, $c = 3.80$ Å), and ($a = 3.82$ Å, $c = 3.80$ Å), respectively. The experimentally available lattice constants for fcc Pt ($a = 3.91$ Å) and L1₀-FePt structures ($a = 3.86$ Å, $c = 3.79$ Å) were found to be very similar to ones obtained through DFT.^{34,35} The plane wave cutoff used for all the geometry optimizations was 450 eV with a $4 \times 4 \times 1$ k-point mesh. A $7 \times 7 \times 7$ k-point mesh was used for lattice constant optimization. All the calculations involving Fe and Co were spin-polarized to account for their ferromagnetic properties. For a given L1₀-MPt alloy (M = Fe or Co), we performed

geometry optimizations on surfaces with varying Pt overlayer thickness, as shown in Fig. 1.

To calculate the eigenforces on the unstrained Pt(111) surface, we took an approach similar to that of Ref. 29. We started off by relaxing a pure Pt(111) bare slab. The optimized slab was fixed and the adsorbate of interest was then added to the surface. The adsorbate was allowed to relax on the surface, while the surface atoms remained fixed. The forces induced by the adsorbate on the neighboring surface atoms were obtained by an atomic force call which gave us the eigenforces introduced on each surface atom. We discuss in Sec. III how these are converted to explicit interaction energies.

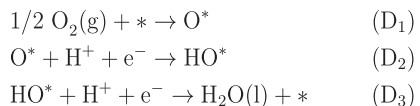
ORR is typically studied via both dissociative and associative mechanism as described in Fig. 2. Based on the scheme shown in Fig. 2, we studied O₂*, HOO*, O*, and HO* as ORR intermediates. Each of these intermediates were adsorbed on their energetically most preferred sites on Pt(111), L1₀-FePt/Pt_n(111), and L1₀-CoPt/Pt_n(111) surfaces ($1 \leq n \leq 4$), as shown in Fig. 3. In the case of L1₀-MPt/Pt₁(111) surfaces, the Pt sites are differentiated by the presence of M atoms in the immediate subsurface. We report all the stable adsorption sites along with their potential energies on L1₀-MPt/Pt₁(111) surfaces in the [supplementary material](#) (See Sec. 2 of the [supplementary material](#)).

We computed the binding energies for the aforementioned reaction intermediates as described by Eq. (1)

$$E_b = E_{S+A} - E_S - E_A, \quad (1)$$

where E_b is the binding energy of an adsorbate, E_{S+A} is the total potential energy of the relaxed slab and adsorbate together, E_S

Dissociative Mechanism



Associative Mechanism

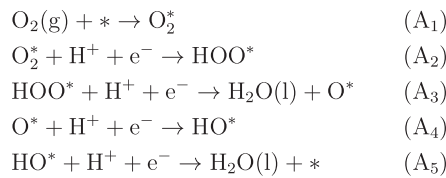


FIG. 2. Elementary steps involved in ORR via dissociative and associative mechanism on a catalyst surface. Note that * represents an adsorption site.

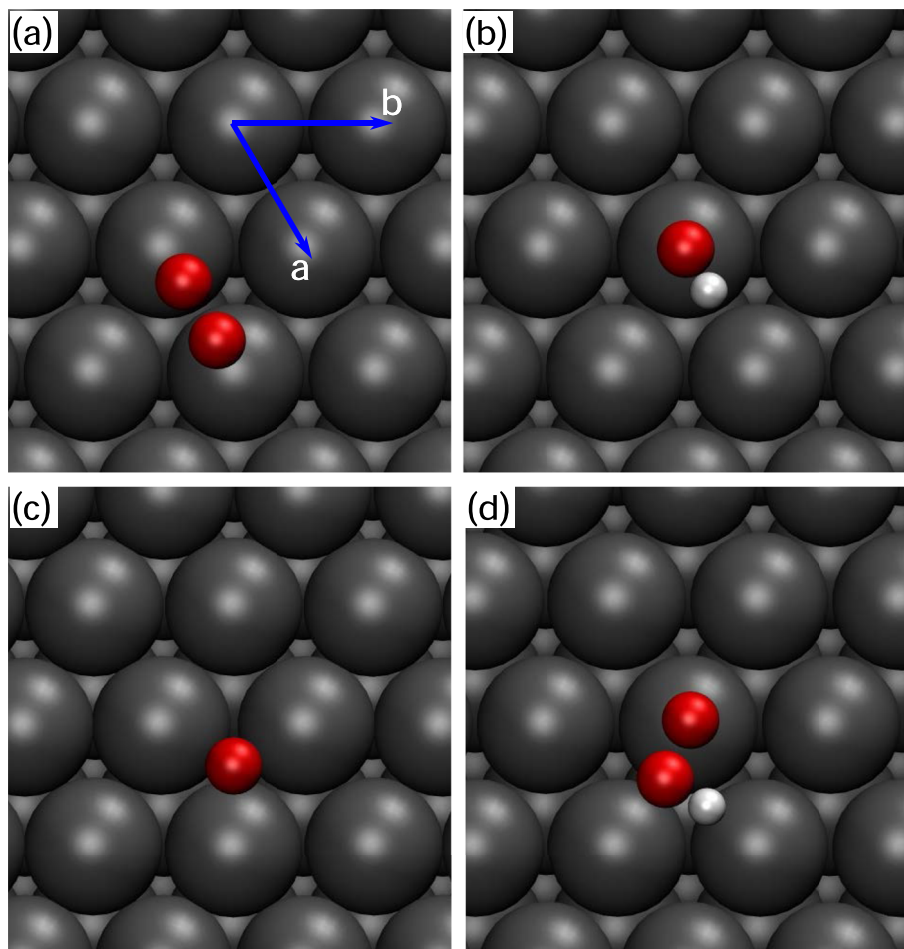


FIG. 3. Energetically most favorable sites for (a) O_2^* , (b) HO^* , (c) O^* , and (d) HOO^* on $Pt(111)$ surface. Note that the adsorption sites remain the same for unstrained $Pt(111)$, $L_{10}-FePt/Pt(111)$, and $L_{10}-CoPt/Pt(111)$ surfaces. The atoms in the descending order of size are Pt, O, and H, respectively.

is the total potential energy of the relaxed slab alone, and E_A is the total gas-phase potential energy of the adsorbate alone. To unify the reference states, the gas-phase potential energies of the adsorbates were referenced to the gas-phase potential energies of H_2O and H_2 . Note that in this convention, more positive values of E_b represent weaker binding.

The computational hydrogen electrode (CHE)⁷ model was used to obtain the reaction free energy of the steps involving a ($H^+ + e^-$) transfer. The CHE model considers the chemical potential of gaseous hydrogen ($\frac{1}{2}\mu[H_2]$) to be equal to the chemical potential of the proton-electron pair ($\mu[H^+] + \mu[e^-]$) at 0 V_{RHE}. (RHE indicates the reversible hydrogen electrode scale.) $\Delta G_U = -eU$ was added to adjust the reaction potential relative to 0 V. The free energy landscapes were obtained at 300 K. The free energies of the gas-phase adsorbates were obtained using the RPBE free energies of H_2O and H_2 and the experimental reaction free energy (2.46 eV) for $H_2O \rightarrow \frac{1}{2}O_2 + H_2$. The ASE thermochemistry module³² was used to calculate the free energies of reaction intermediates, where gases were treated in the ideal-gas limit and adsorbates were treated in the harmonic limit.

III. RESULTS AND DISCUSSION

A. Structural effects on binding strengths

We start off by investigating how the Pt skin structure affects the binding strength of the ORR intermediates, decoupling the strain and ligand effects. Figures 4 and 5 show the binding energies for the adsorbed intermediates (O_2^* , HOO^* , O^* , and HO^*) on $L_{10}-FePt/Pt(111)$ and $L_{10}-CoPt/Pt(111)$, respectively, with varying thickness of Pt overlayers. The positive “sign” of binding energies for HOO^* , HO^* , and O^* are due to the choice of gas phase reference states as described under the computational details. The positive “sign” does not signify repulsive interactions. A black horizontal line indicates the binding energy of the reaction intermediates on the unstrained $Pt(111)$ surface. We observe that the reaction intermediates bind weakly on these Pt skin surfaces as compared to that on unstrained fcc $Pt(111)$, due to a coupled strain and ligand effect. We can decouple this effect by also examining a pure strain effect, through calculating binding energies on pure Pt structures at the same strain levels as the fcc structures. This allows a separation of the strain and

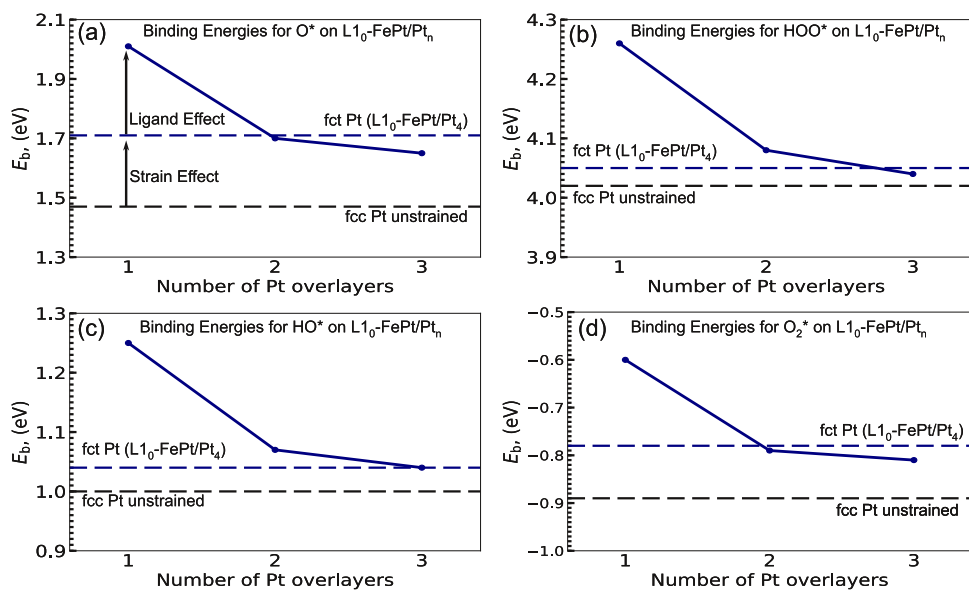


FIG. 4. Binding energies of (a) O^* , (b) HOO^* , (c) HO^* , and (d) O_2^* on $L1_0\text{-FePt}/Pt$ with varying thickness of Pt over-layers. The face-centered tetragonal (fct) Pt ($L1_0\text{-FePt}/Pt_4$) and fcc Pt unstrained represent Pt slabs with the lattice parameters of $L1_0\text{-FePt}$ and native Pt, respectively.

ligand effects. As expected, the ligand effect decays with an increasing thickness of Pt overlayers, and the binding energies fall asymptotically until only the strain effect remains. The $L1_0\text{-CoPt}/Pt$ experiences an in-plane biaxial strain of -4.50% along [011] (the a direction) and -4.25% along [110] (the b direction) with respect to unstrained Pt. On the other hand, $L1_0\text{-FePt}/Pt$ experiences a strain of -3.47% and -2.23% along [011] and [110], respectively. (The negative sign indicates the strain is compressive.) Note that the surface strain is slightly anisotropic, as it is a cut of the bulk fct structure which is also compressed anisotropically relative to the pure unstrained fcc Pt system; this is explained in Fig. S1 of the [supplementary material](#).

B. Free energy landscapes and limiting potentials

I. Dissociative mechanism

Figure 6 shows the free energy landscape at $U = 1.23$ V_{RHE} via dissociative mechanism on $L1_0\text{-FePt}/Pt(111)$, $L1_0\text{-CoPt}/Pt(111)$ surfaces with varying thickness of Pt over-layers. Here, U is the electrode potential versus RHE. For all the surfaces considered, we observe that the step involving formation of O^* (D_1) is downhill in free energy (i.e., exergonic), while the following two protonation steps of O^* and HO^* (D_2 and D_3) are uphill in free energy (i.e., endergonic). The potential at which the entire free energy surface becomes completely exergonic is conventionally considered

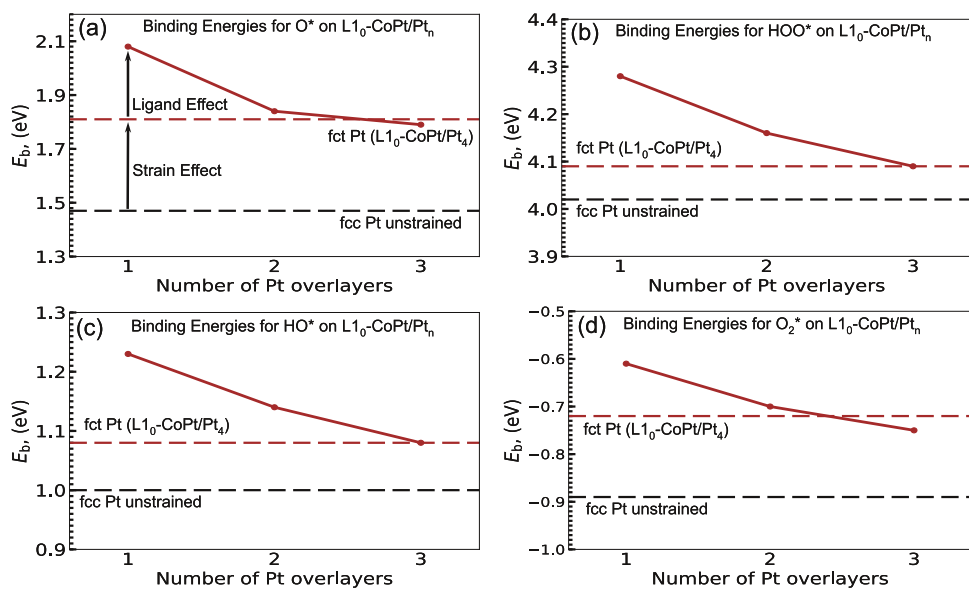


FIG. 5. Binding energies of (a) O_2^* , (b) HOO^* , (c) O^* , and (d) HO^* on $L1_0\text{-CoPt}/Pt$ as a function of Pt over-layers. The fcc Pt ($L1_0\text{-CoPt}/Pt_4$) and fcc Pt unstrained represent Pt slabs with the lattice parameters of $L1_0\text{-CoPt}$ and native Pt, respectively.

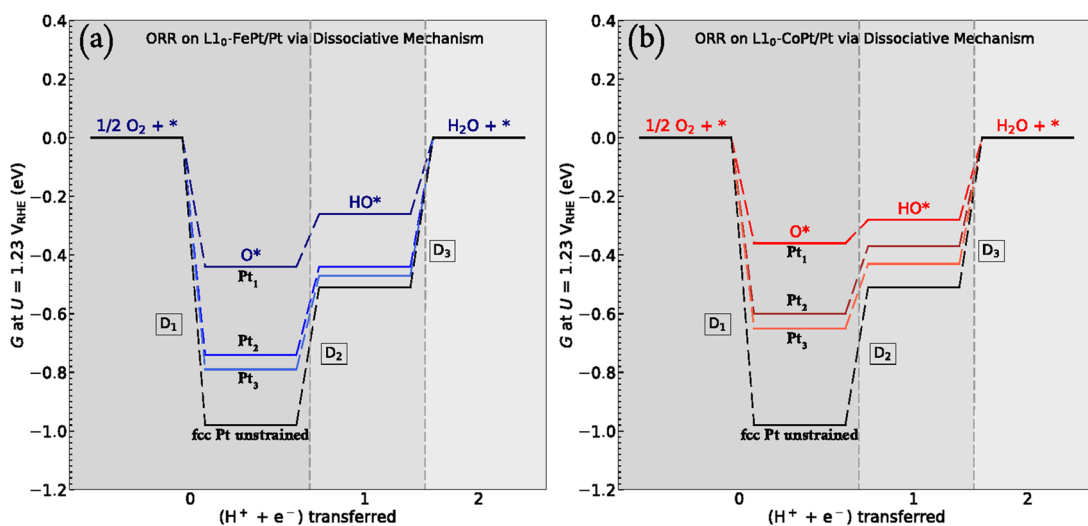


FIG. 6. Free energy diagrams at $U = 1.23$ V for oxygen reduction reactions via dissociative mechanism on (a) $\text{L1}_0\text{-FePt}/\text{Pt}_n$ and (b) $\text{L1}_0\text{-CoPt}/\text{Pt}_n$ where ($n = 1, 2, 3$).

as the limiting potential (U_L), which we take as a proxy for the onset potential. Since both the protonation steps (D_2 and D_3) involved are potential-dependent, the free energy landscape can be made entirely downhill by lowering the potential of the electrode by an amount equal to the larger of the two thermodynamic barriers, ΔG_L (D_2 or D_3). We consider the thermodynamically required overpotential (η) as $\Delta G_L/e$. Here, e is the charge of an electron. The new potential at which the free energy landscape now becomes completely exergonic is called the limiting potential (U_L) and is given by

$$\eta = 1.23 - U_L = \Delta G_L/e. \quad (2)$$

U_L is commonly used to correlate with experimental onset potentials and is considered a reasonable choice to use as an ORR activity indicator.^{36–38} More positive limiting potentials (U_L) indicate lower overpotential requirements to achieve a given current density, or equivalently better ORR activity at a specified overpotential. We observe that the strain and/or ligand effect on $\text{L1}_0\text{-FePt}/\text{Pt}(111)$ and $\text{L1}_0\text{-CoPt}/\text{Pt}(111)$ surfaces destabilizes the ORR reaction intermediates by raising their free energies, as shown in Fig. 6. The destabilization results in lower overpotential (η) or higher limiting potential (U_L) on $\text{L1}_0\text{-FePt}/\text{Pt}(111)$ and $\text{L1}_0\text{-CoPt}/\text{Pt}(111)$ surfaces compared to unstrained Pt(111) surface, as shown in Fig. 7. For all the surfaces considered, we observe that D_3 is the potential limiting step since it has the maximum positive change in free energy. The change in free energies associated with each step in dissociative mechanism are provided in Tables I and II for $\text{L1}_0\text{-FePt}/\text{Pt}(111)$ and $\text{L1}_0\text{-CoPt}/\text{Pt}(111)$ surfaces, respectively. We observe that decreasing the number of Pt overlayers makes the reaction intermediates less stable by raising their free energies due to the increasing ligand effect. For ~ 3 or more

Pt overlayers, it is dominantly the strain effect which controls the binding strength of a reaction intermediate and the change in free energies associated with each step of the reaction mechanism. Note that the ligand effect is observed to be more on $\text{L1}_0\text{-FePt}/\text{Pt}(111)$ surfaces than in $\text{L1}_0\text{-CoPt}/\text{Pt}(111)$ as evident from Fig. 7 for Pt overlayer thickness of 1. On the other hand, $\text{L1}_0\text{-CoPt}/\text{Pt}(111)$ experiences higher compressive strain compared to $\text{L1}_0\text{-FePt}/\text{Pt}(111)$. Hence, for thicker Pt overlayers, $\text{L1}_0\text{-CoPt}/\text{Pt}(111)$ shows higher calculated ORR activity as compared to both $\text{L1}_0\text{-FePt}/\text{Pt}(111)$ and unstrained fcc Pt(111) surfaces.

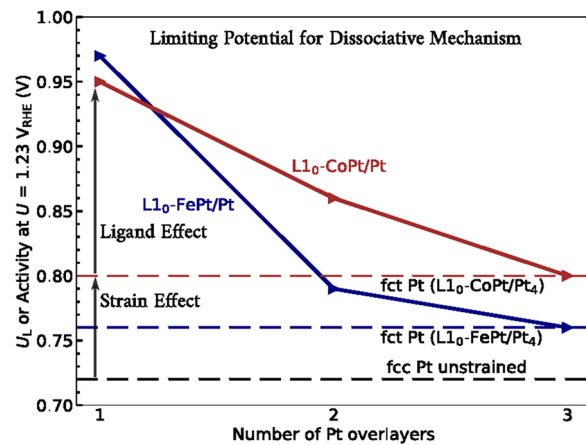


FIG. 7. Activity in terms of limiting potential (U_L) at $U = 1.23$ V for ORR in dissociative mechanism for both $\text{L1}_0\text{-FePt}/\text{Pt}_n$ and (b) $\text{L1}_0\text{-CoPt}/\text{Pt}_n$ where ($n = 1, 2, 3$). The fcc Pt ($\text{L1}_0\text{-CoPt}/\text{Pt}_4$), fcc Pt ($\text{L1}_0\text{-FePt}/\text{Pt}_4$) and fcc Pt unstrained represents Pt slabs with the lattice parameters of $\text{L1}_0\text{-CoPt}$, $\text{L1}_0\text{-FePt}$ and native Pt, respectively.

TABLE I. Comparison between calculated change in free energies for the steps in dissociative mechanism over $\text{L}_{10}\text{-FePt}$ and unstrained fcc Pt.

System	D_1 (eV)	D_2 (eV)	D_3 (eV)	U_L (V)
$\text{L}_{10}\text{-FePt}/\text{Pt}_1$	-0.44	0.17	0.26	0.97
$\text{L}_{10}\text{-FePt}/\text{Pt}_2$	-0.74	0.30	0.44	0.79
$\text{L}_{10}\text{-FePt}/\text{Pt}_3$	-0.79	0.32	0.47	0.76
$\text{L}_{10}\text{-FePt}/\text{Pt}_4$	-0.73	0.26	0.47	0.76
fcc Pt (unstrained)	-0.98	0.46	0.51	0.72

TABLE II. Comparison between calculated change in free energies for the steps in dissociative mechanism over $\text{L}_{10}\text{-CoPt}$ and unstrained fcc Pt.

System	D_1 (eV)	D_2 (eV)	D_3 (eV)	U_L (V)
$\text{L}_{10}\text{-CoPt}/\text{Pt}_1$	-0.36	0.08	0.28	0.95
$\text{L}_{10}\text{-CoPt}/\text{Pt}_2$	-0.60	0.23	0.37	0.86
$\text{L}_{10}\text{-CoPt}/\text{Pt}_3$	-0.65	0.22	0.43	0.80
$\text{L}_{10}\text{-CoPt}/\text{Pt}_4$	-0.63	0.20	0.43	0.80
fcc Pt (unstrained)	-0.98	0.46	0.51	0.72

We also consider an alternate route to form H_2O via the disproportionation reaction of $\text{HO}^* + \text{HO}^*$ to give $\text{H}_2\text{O} + \text{O}^*$ instead of the protonation of HO^* to H_2O (Step D_3 or A_5 in Fig. 2). Although the formation of H_2O through the disproportionation reaction route seems feasible for unstrained fcc Pt(111), it is expected to have much lower rate on $\text{L}_{10}\text{-MPt}/\text{Pt}_n$ surfaces at 300 K, as discussed in Sec. 3 of the [supplementary material](#). Hence, we only consider formation of H_2O through protonation of HO^* for the rest of the discussion. Figure S3 of the [supplementary material](#) shows the free energy landscape for H_2O formation through the disproportionation reaction on both $\text{L}_{10}\text{-FePt}/\text{Pt}_n$ and $\text{L}_{10}\text{-CoPt}/\text{Pt}_n$ surfaces. The change in free energies associated with each step in dissociative mechanism proceeding through disproportionation reaction to form H_2O is also provided in Tables S3 and S4 of the [supplementary material](#).

2. Associative mechanism

The free energy landscapes for ORR via the associative mechanism with varying thicknesses of Pt overlayers are shown in Fig. 8. All four intermediates are destabilized on $\text{L}_{10}\text{-FePt}/\text{Pt}(111)$ and $\text{L}_{10}\text{-CoPt}/\text{Pt}(111)$ surfaces as compared to unstrained fcc Pt(111) surface. Similar to the effect in dissociative mechanism, we see that the ligand effect further destabilizes the intermediates as we decrease the Pt overlayers. Unlike the dissociative mechanism, which has only two endergonic steps (i.e., protonation of O^* and of HO^*), the associative mechanism has three endergonic steps (i.e., protonation of O_2^* , O^* , and HO^*). We find the change in free energy in the O_2^* protonation step to be the highest for all our systems, which gives us the limiting potential, U_L , for the associative mechanism. The changes in free energies associated with each step in the associative mechanism are provided in Tables III and IV. We observe that ORR activity increases via the associative mechanism on both $\text{L}_{10}\text{-FePt}/\text{Pt}(111)$ and $\text{L}_{10}\text{-CoPt}/\text{Pt}(111)$ surfaces compared to unstrained fcc Pt (see Fig. 9), similar to that observed in the dissociative mechanism.

Since the focus of this work is restricted only to the elementary thermodynamics associated with both mechanisms, we avoid drawing conclusions on the kinetic feasibility and dominance of one mechanism over the other. For example, we can estimate the activation barrier required for O-O bond dissociation with a linear transition-state adsorbate scaling relation ($E_a = 1.8 E_b(\text{O}^*) - 2.89$) as described by Karlberg *et al.*,³⁶ which we find to be 0.73 eV and 0.85 eV for $\text{L}_{10}\text{-FePt}/\text{Pt}_1$ and $\text{L}_{10}\text{-CoPt}/\text{Pt}_1$ surfaces, respectively. At this stage, the dominance of either O_2^* dissociation or O_2^* protonation becomes the deciding factor governing the ORR mechanism. In order to confidently predict the feasibility and dominance of one mechanism over the other we need to conduct a potential-dependent kinetic barrier study, which we intend to address in future work.

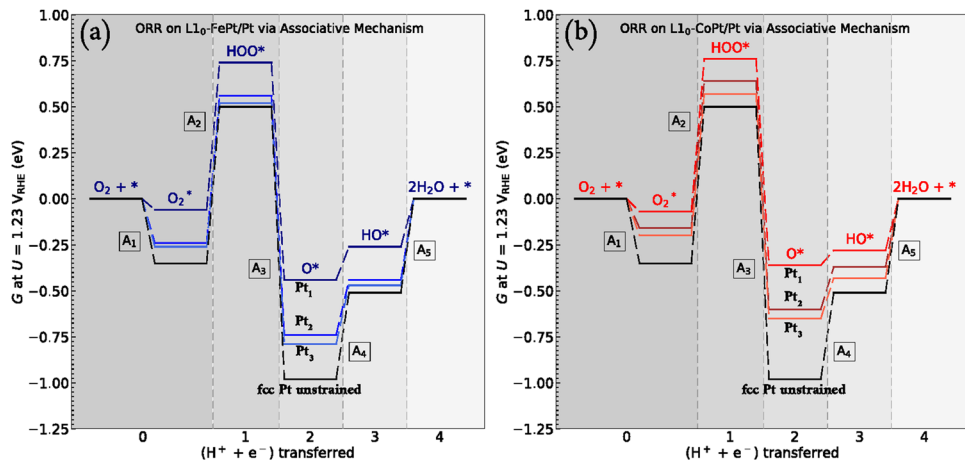


FIG. 8. Free energy diagrams at $U = 1.23$ V for oxygen reduction reactions via associative mechanism on (a) $\text{L}_{10}\text{-FePt}/\text{Pt}_n$ and (b) $\text{L}_{10}\text{-CoPt}/\text{Pt}_n$ where ($n = 1, 2, 3$).

TABLE III. Comparison between calculated change in free energies for the steps in associative mechanism on L1₀-FePt/Pt and unstrained Pt.

System	A ₁ (eV)	A ₂ (eV)	A ₃ (eV)	A ₄ (eV)	A ₅ (eV)	U _L (V)
L1 ₀ -FePt/Pt ₁	-0.06	0.80	-1.18	0.17	0.26	0.43
L1 ₀ -FePt/Pt ₂	-0.24	0.81	-1.30	0.30	0.44	0.42
L1 ₀ -FePt/Pt ₃	-0.26	0.78	-1.31	0.32	0.47	0.45
L1 ₀ -FePt/Pt ₄	-0.23	0.77	-1.27	0.26	0.47	0.46
fcc Pt (unstrained)	-0.35	0.85	-1.48	0.46	0.51	0.38

C. Rationalizing strain effects via an eigenstress model

The eigenstress model introduced by Khorshidi et al.²⁹ provides an intuitive way to characterize the binding behavior of an adsorbate with applied strain. According to the model, any perturbation caused by the presence of an adsorbate on a small region of volume V_I acting as a subdomain of a continuous body can induce an eigenstress σ^* (a tensor) on the subdomain surface boundary. The eigenstress is positive if the adsorbate pushes the neighboring surface atoms outwards or negative if it pulls them inwards. At an arbitrary applied external strain ϵ^0 (a tensor), the binding energy of an adsorbate can be further calculated as

$$E_b(\epsilon^0) = E_b(0) + E_{\text{int}}(\epsilon^0, \sigma^*), \quad (3)$$

where $E_b(0)$ is the binding energy of an adsorbate at zero applied strain and E_{int} is the interaction potential energy of the applied external strain with the induced eigenstress. Note that a more positive value of $E_b(\epsilon^0)$ indicates weaker binding. The interaction potential energy, E_{int} is calculated as

$$E_{\text{int}} = - \int_{V_I} \sum_{i,j} [\epsilon_{ij}^0(x) \sigma_{ij}^*(x)] dx. \quad (4)$$

The above equation is exact in the limit of linear elasticity. Here, ϵ_{ij}^0 and σ_{ij}^* represent the tensorial components of ϵ^0 and σ^* , respectively. Based on the sign of the interaction energy, E_{int} , we can qualitatively predict the response of binding energy to the applied strain. In other words,

$$E_b(\epsilon^0) : \begin{cases} > E_b(0) & \text{if } - \sum_{i,j} \epsilon_{ij}^0 \sigma_{ij}^* > 0, \\ < E_b(0) & \text{if } - \sum_{i,j} \epsilon_{ij}^0 \sigma_{ij}^* < 0. \end{cases} \quad (5)$$

As seen from the schematic in Fig. 10, the ORR reaction intermediates tend to push the atoms outwards (positive eigenstress). This suggests that applying a compressive external strain should result in a more positive binding energy, that

TABLE IV. Comparison between calculated change in free energies for the steps in associative mechanism on L1₀-CoPt/Pt and unstrained Pt.

System	A ₁ (eV)	A ₂ (eV)	A ₃ (eV)	A ₄ (eV)	A ₅ (eV)	U _L (V)
L1 ₀ -CoPt/Pt ₁	-0.07	0.83	-1.12	0.08	0.28	0.40
L1 ₀ -CoPt/Pt ₂	-0.16	0.80	-1.24	0.23	0.37	0.43
L1 ₀ -CoPt/Pt ₃	-0.20	0.77	-1.22	0.22	0.43	0.46
L1 ₀ -CoPt/Pt ₄	-0.17	0.75	-1.21	0.20	0.43	0.48
fcc Pt (unstrained)	-0.35	0.85	-1.48	0.46	0.51	0.38

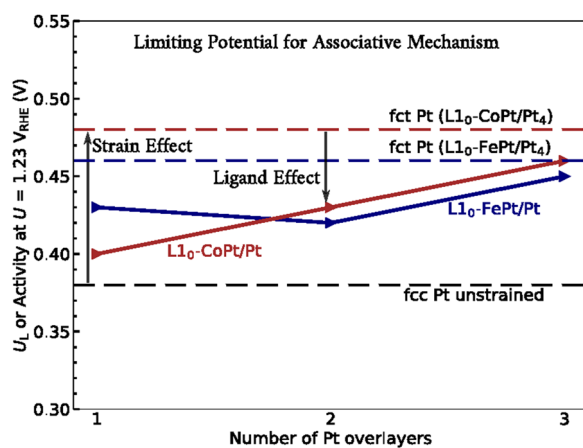


FIG. 9. Activity in terms of limiting potential (U_L) at $U = 1.23$ V for ORR in associative mechanism for both L1₀-FePt/Pt_n and (b) L1₀-CoPt/Pt_n where ($n = 1, 2, 3$). The fct Pt (L1₀-CoPt/Pt₄), fct Pt (L1₀-FePt/Pt₄) and fcc Pt unstrained represent Pt slabs with the lattice parameters of L1₀-CoPt, L1₀-FePt, and native Pt, respectively.

is, weakening the binding. On the other hand, a tensile external strain should result in stronger binding. Both L1₀-FePt/Pt(111) and L1₀-CoPt/Pt(111) experience a biaxial compressive strain as compared to the unstrained Pt(111) surface. Hence, the eigenstress model predicts weaker binding strength of the reaction intermediates on L1₀-FePt/Pt₄(111) and L1₀-CoPt/Pt₄(111) as compared to the unstrained fcc Pt(111) surface, as observed in Figures 4 and 5.

The eigenstress model has shown that the interaction potential energy can be described by the coupling between the adsorbate induced surface stress with the applied external strain. However, quantitatively assigning continuum properties, like stress and strain, in an atomistic model is challenging. As a refinement to the eigenstress model, here we suggest an eigenforce model to calculate the interaction energy, E_{int} , using discrete atomistic inputs. According to the eigenforce model, the interaction energy is considered as the integral of induced eigenforces times displacement over each atom, rather than the contribution of each stress and strain component on the surface (Fig. 11). Here, displacement refers to the change in the Cartesian coordinate of an individual atom due to the applied strain. The interaction energy described by the eigenforce model is of the form

$$E_{\text{int}} = \sum_{i \in S} \int \mathbf{F}_i d\mathbf{R}_i, \quad (6)$$

where \mathbf{R}_i is the Cartesian coordinate of the atom i and \mathbf{F}_i is the force on the corresponding surface atom induced by relaxing an adsorbate on a fixed unstrained surface. This integral is applied on all the atoms of the surface (S). For convenience, the above equation can be further simplified by assuming that the eigenforce remains constant with strain. Then the equation can be reduced to

$$E_{\text{int}} \approx - \sum_{i \in S} \mathbf{F}_i \Delta \mathbf{R}_i. \quad (7)$$

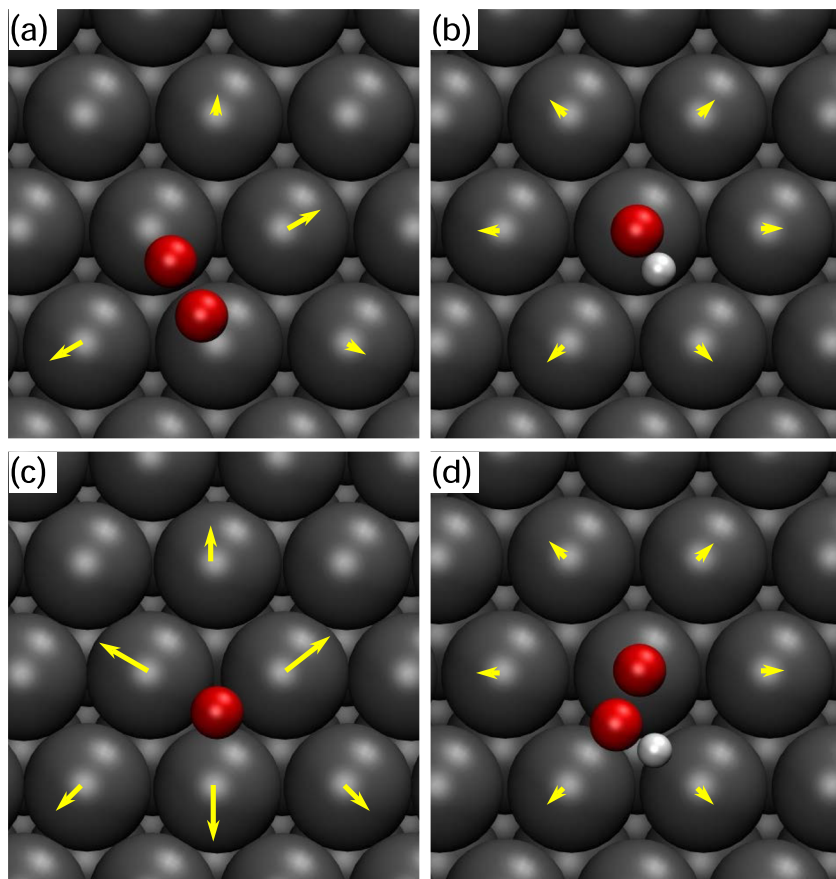


FIG. 10. In plane components of forces on the surface atoms on native Pt(111) surface atoms induced by (a) O_2^* , (b) HO^* , (c) O^* , and (d) HOO^* . The eigenforces, as vectors, for each of the cases are provided in the supplementary material.

This, of course, introduces a systematic second-order error into the equation since forces opposed to a displacement will tend to increase with the displacement, while forces inline with a displacement will tend to decrease. Here the

displacement $\Delta\mathbf{R}_i$ is given by the change of the Cartesian coordinate of the surface atoms with applied strain. Hence, the eigenforce model uses $\Delta\mathbf{R}_i$ and \mathbf{F}_i to calculate E_{int} without explicitly performing electronic structure calculations on strained surfaces.

The eigenforce model justifies the weaker binding of the reaction intermediates on $L1_0$ -CoPt/Pt₄(111) than on $L1_0$ -FePt/Pt₄(111) since the former experiences a higher compressive strain along both [011] and [110] directions. Figure 10 shows that the intermediates O_2^* and O^* induce relatively higher eigenforce on the neighboring surface atoms as shown by the magnitude of the in-plane components of forces on the surface atoms (lengths of the arrows) as compared to the eigenforce induced by the presence of HOO^* and HO^* intermediates. This is in accordance with the DFT calculations as shown in Figures 4 and 5.

We compare the calculated interaction energy with the actual change in the binding energy of the ORR intermediates on $L1_0$ -CoPt/Pt₄(111) and $L1_0$ -FePt/Pt₄(111) surfaces with respect to unstrained fcc Pt(111), as shown by a parity plot in Fig. 12. The results obtained from DFT calculations very well follow the trend predicted by the eigenforce model; i.e., more positive interaction energy leads to weaker binding. We observe that the eigenforce model over-predicts the change in

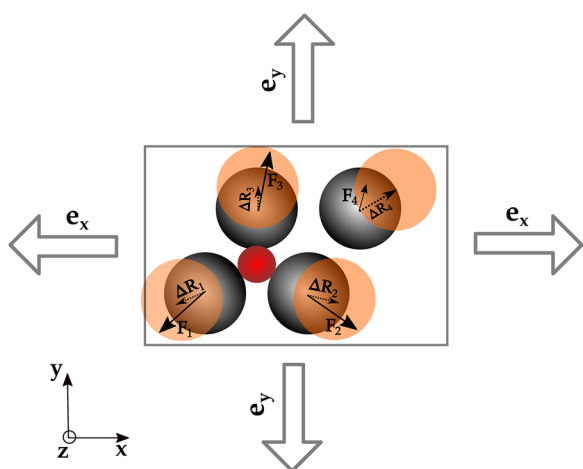


FIG. 11. Schematic showing in plane components of the adsorbate induced eigenforces and displacement due to applied strain.

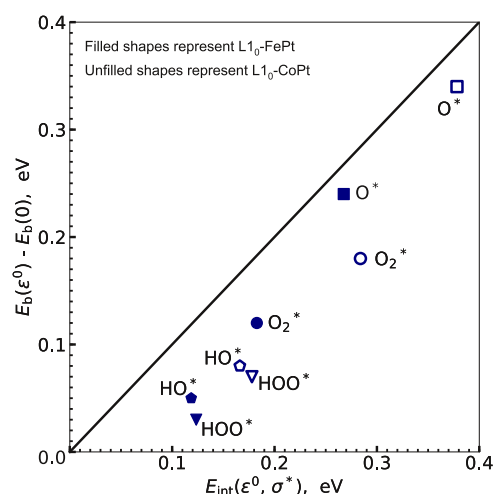


FIG. 12. Interaction energy, E_{int} versus the actual change in binding energies on $\text{L1}_0\text{-FePt}/\text{Pt}$ (filled shapes) and $\text{L1}_0\text{-CoPt}/\text{Pt}$ (unfilled shapes).

binding energy since all the data points fall below the diagonal of the parity plot. The over-prediction of the change in binding energy by the eigenforce model is believed to be due to fewer degrees of freedom provided to the system during relaxation for the calculation of eigenforces (where only the adsorbate was allowed to relax) as compared to the calculation of actual binding energies (where both the adsorbate and the slab were allowed to relax).

D. Optimum strain range for ORR using eigenforce model

We further use the eigenforce model to predict the change in binding energy of ORR intermediates with different applied compressive strains. Table V shows the calculated interaction energy with applied equi-biaxial compressive strain on the Pt(111) surface. Theoretical studies have proposed that a good ORR catalyst should bind O^* (0.0–0.4 eV weaker) and HO^* (0.0–0.2 eV weaker) compared to the unstrained Pt(111) surface.^{19,20} The interaction energies obtained from the eigenstress model can be treated as the upper-bound in the expected change in the binding energy of the ORR reaction intermediates with applied compressive strain. The eigenstress model is in agreement with the conventional d-band center model suggesting weaker binding of the ORR reaction intermediates with applied compressive strain. It has also been

experimentally reported that biaxial strain of around −4% to −5% on Pt(111) overlayers fall in the optimum ORR activity range with HO^* binding weakened by (~0.10–0.15 eV) as confirmed from DFT.²⁷ This is in agreement with the eigenforce model which approximately predicts a similar change in HO^* binding energy (considering the over prediction of around ~0.08 eV in the change in binding energy by the eigenforce model) with applied compressive strain on Pt(111) overlayers, as shown in Table V.

We construct the free energy landscapes by converting the binding energies obtained from the eigenforce model to free energies. Figure 13 shows that the predicted free energy landscape on Pt(111) via both dissociative and associative mechanism with varying biaxial compressive strain. We observe that the eigenforce model is able to predict similar trends observed from our DFT calculations; i.e., an upward shift in the free energy of each reaction intermediate with increasing values of applied compressive strain.

We highlight that $\text{L1}_0\text{-FePt}/\text{Pt}_4$ and $\text{L1}_0\text{-CoPt}/\text{Pt}_4$ sit in one continuous trend with a biaxial compressive strain of −3.47%/-2.23% and −4.50%/-4.25%, respectively, along [011]/[110] directions, as shown in Fig. 13. The eigenforce model roughly suggests that further application of compressive strain on the Pt(111) surface (~−5% or more) will lead to further weakening of ORR intermediates like O_2^* and O^* . Too weak binding of the reaction intermediates will reduce the ability of the catalyst surface to activate O_2 ($\text{O}_2 \rightarrow \text{O}_2^*$ being uphill in free energy as shown in Fig. 13) as well as limiting the occurrence of ORR due to too weak binding of O^* (ΔE_b for O^* greater than 0.4 eV) as observed in literatures.^{19,20} For compressive strain greater than −5%, we observe that the adsorption of O_2 becomes uphill in free energy as shown in Fig. 13. The overall change in free energy, ΔG , required for the reaction to be completely exergonic for compressive strain greater than −5% is given by the sum of the uphill change in free energy for the O_2 adsorption step and the overpotential, η , for both dissociative and associative mechanisms, respectively. Note that dissociative mechanism also requires the activation of O_2 for further dissociation to O^* . For compressive strain of ~−5% or less, the ΔG equals the overpotential, η . The required change in free energy, ΔG , corresponding to different strain levels for both dissociative and associative mechanisms are shown in Table VI. We observe that ΔG is minimum for −5% compressive strain for both associative and dissociative mechanism. The numerical values of the overpotential obtained from the eigenforce model are found to be very close to the ones obtained from our DFT results (less than ~0.1 eV difference). We observe that the overpotential, η obtained for $\text{L1}_0\text{-CoPt}/\text{Pt}_4$ falls very close to that obtained from the Pt(111) surface having an equi-biaxial strain of −5%. This suggests that $\text{L1}_0\text{-CoPt}/\text{Pt}_4$ may show near optimum behavior for ORR activity as predicted by the eigenforce model. The actual change in binding energy for HO^* on the $\text{L1}_0\text{-CoPt}/\text{Pt}_4(111)$ surface is found to be ~0.1 eV which is reported as the near ideal change in HO^* for optimum ORR activity by many previous theoretical studies.^{7,19,20,39}

TABLE V. Interaction energy, E_{int} (eV) with the applied equi-biaxial strain on the Pt(111) surface. Note that positive interaction energy suggests weaker binding.

Adsorbate	−1%	−2%	−3%	−4%	−5%	−6%	−7%
O_2^*	0.07	0.13	0.20	0.26	0.33	0.38	0.46
HOO^*	0.04	0.08	0.12	0.16	0.20	0.24	0.28
HO^*	0.04	0.08	0.11	0.15	0.18	0.23	0.26
O^*	0.09	0.17	0.26	0.34	0.43	0.51	0.60

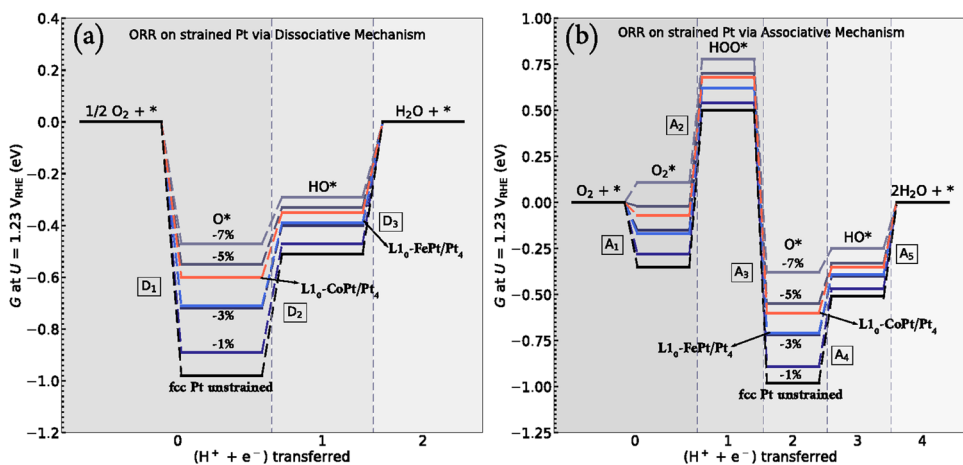


FIG. 13. Free energy diagrams at $U = 1.23 \text{ V}_{\text{RHE}}$ for oxygen reduction reaction on the Pt(111) surface with varying compressive strain via (a) dissociative mechanism and (b) associative mechanism. L1₀-CoPt/Pt₄, L1₀-FePt/Pt₄ and fcc Pt unstrained represents Pt slabs with the lattice parameters of L1₀-CoPt, L1₀-FePt, and native Pt, respectively.

TABLE VI. The change in free energy (ΔG) required to make the reaction pathway downhill for both dissociative and associative mechanisms with varying compressive strain as obtained from the eigenforce model.

Strain %	Dissociative mechanism	Associative mechanism
	ΔG (eV)	ΔG (eV)
Unstrained Pt	0.51	0.85
-1%	0.47	0.82
L1 ₀ -FePt/Pt ₄	0.39	0.79
-3%	0.40	0.77
L1 ₀ -CoPt/Pt ₄	0.35	0.75
-5%	0.33	0.72
-6%	0.34	0.74
-7%	0.37	0.79

IV. CONCLUSIONS

In conclusion, our study has shown that L1₀-FePt/Pt and L1₀-CoPt/Pt are promising candidates for ORR catalysts. The ORR reaction intermediates are found to bind weakly on the L1₀-FePt/Pt and L1₀-CoPt/Pt surfaces as compared to the unstrained fcc Pt(111) surface. The free energy landscapes have shown that both L1₀-FePt/Pt and L1₀-CoPt/Pt systems have higher calculated ORR activity via both associative and dissociative mechanism. Depending upon the thickness of the Pt overlayer, the strain or ligand may dominate the effect on ORR activity. For Pt overlayer thickness of around three or more atomic layers, the strain effect is found to be dominant. Note that in a real system, if the number of Pt overlayers continues to increase, we would expect the strain effect to eventually die out. Such relaxation occurs due to a variety of effects, such as grain boundaries, defects, or particle curvature, all of which are difficult to assess with electronic structure calculations.

Deconvolution of the strain from the ligand effect is a difficult task to perform experimentally as they both may co-occur. On the other hand, using electronic structure theory, we can approximately separate one effect from the other as shown in this study. Our method describes a way to

approximately determine the effectiveness of one effect over the other based on the Pt shell thickness. Depending on the nature of the ligand and its relative position to the Pt shell, we can further estimate its effect on the ORR activity. For a Pt shell thickness of ~1, we observe the ligand effect to be the most important in deciding the fate of the ORR activity. However, in a real case system, we are more likely to observe a slightly thicker shell where strain and ligand effects may co-exist. This provides a great tool for the experimental community to decide on the required Pt shell thickness for the optimum use of a particular M_xPt_{1-x} catalyst depending on the effectiveness of the compressive strain with or without the presence of the ligand effect.

We further show that the proposed intuitive eigenforce model is able to give a (semi-) quantitative prediction of the binding energy change due to a pure strain effect. The trends observed by the eigenforce model are in agreement with the conventional d-band center model. The calculated interaction energy, E_{int} , can be used as a descriptor to study the response of applied strain on the binding strengths of the ORR reaction intermediates.

Finally, we use the eigenforce model to predict the experimentally observed ideal compressive strain range for optimum ORR performance on the Pt(111) surface. We observe a very clear trend in the change in binding energies of the reaction intermediates with applied strain suggesting that compressive strain of around -5% would show near ideal ORR behavior.

The stability of the solute metal in a M_xPt_{1-x} alloy is an important factor governing the influence of the strain and/or ligand on the surface activity of the catalyst. Efficient stabilization of the solute metal will not only prevent leaching of Fe/Co into the electrolyte but also preserve the strained surface in the long term. Experimental results on L1₀-FePt by Li et al.²⁸ have shown improved stabilization of Fe in the alloy with a thin Pt shell of ~2 overlayer thickness suggesting that strain and ligand effects may occur simultaneously. Hence, stabilization of

Fe/Co can further preserve the ligand effect for further tuning of the ORR activity. Electronic structure theory calculations can be employed to understand the long term stability of MPt alloys which otherwise are difficult to measure experimentally. Studying stability as a function of the alloying element and Pt shell thickness will further help us predict the number of Pt overlayers to expect, which greatly decides the effect influencing the ORR surface activity.

SUPPLEMENTARY MATERIAL

See [supplementary material](#) for the procedure used to determine the anisotropic lattice contraction of the alloys (Sec. 1), energetically stable binding sites for adsorbates on the alloy surfaces (Sec. 2), alternate pathway for water formation through the disproportionation reaction (Sec. 3), and eigenforces on each atom and the optimized geometry for the surfaces considered in the eigenforce model analysis (Sec. 4).

ACKNOWLEDGMENTS

The authors are grateful for financial support for this project from the U.S. Department of Energy Fuel Cell Technologies Office and the support of Program Manager Nancy Garland. The authors would also like to thank Shouheng Sun, Jacob S. Spendelow, Georg Kastlunger, Alireza Khorshidi, and Junrui Li, for fruitful discussions and advice. Electronic structure calculations were carried out at Brown University's Center of Computation and Visualization (CCV).

REFERENCES

- ¹U. Eberle, B. Müller, and R. von Helmolt, "Fuel cell electric vehicles and hydrogen infrastructure: Status 2012," *Energy Environ. Sci.* **5**, 8780 (2012).
- ²J. O. Bockris, "A hydrogen economy," *Science* **176**, 1323 (1972).
- ³G. Marbán and T. Valdés-Solís, "Towards the hydrogen economy?," *Int. J. Hydrogen Energy* **32**, 1625–1637 (2007).
- ⁴R. Shinnar, "The hydrogen economy, fuel cells, and electric cars," *Technol. Soc.* **25**, 455–476 (2003).
- ⁵M. J. Janik, C. D. Taylor, and M. Neurock, "First-principles analysis of the initial electroreduction steps of oxygen over Pt(111)," *J. Electrochem. Soc.* **156**, B126 (2009).
- ⁶J. Greeley, I. E. L. Stephens, A. S. Bondarenko, T. P. Johansson, H. A. Hansen, T. F. Jaramillo, J. Rossmeisl, I. Chorkendorff, and J. K. Nørskov, "Alloys of platinum and early transition metals as oxygen reduction electrocatalysts," *Nat. Chem.* **1**, 552–556 (2009).
- ⁷J. K. Nørskov, J. Rossmeisl, A. Logadottir, L. Lindqvist, J. R. Kitchin, T. Bligaard, and H. Jónsson, "Origin of the overpotential for oxygen reduction at a fuel-cell cathode," *J. Phys. Chem. B* **108**(46), 17886–17892 (2004).
- ⁸D. Wang, H. L. Xin, R. Hovden, H. Wang, Y. Yu, D. A. Muller, F. J. Disalvo, and H. D. Abruna, "Structurally ordered intermetallic platinum–cobalt core-shell nanoparticles with enhanced activity and stability as oxygen reduction electrocatalysts," *Nat. Mater.* **12**, 81–87 (2013).
- ⁹X. Huang, Z. Zhao, L. Cao, Y. Chen, E. Zhu, Z. Lin, M. Li, A. Yan, A. Zettl, Y. M. Wang, X. Duan, T. Mueller, and Y. Huang, "ELECTROCHEMISTRY. High-performance transition metal-doped Pt₃Ni octahedra for oxygen reduction reaction," *Science* **348**, 1230–1234 (2015).
- ¹⁰Z. Duan and G. Wang, "A first principles study of oxygen reduction reaction on a Pt(111) surface modified by a subsurface transition metal M (M = Ni, Co, or Fe)," *Phys. Chem. Chem. Phys.* **13**, 20178 (2011).
- ¹¹J. R. Kitchin, J. K. Nørskov, M. A. Bartea, and J. G. Chen, "Role of strain and ligand effects in the modification of the electronic and chemical properties of bimetallic surfaces," *Phys. Rev. Lett.* **93**, 156801 (2004).
- ¹²J. R. Kitchin, J. K. Nørskov, M. A. Bartea, and J. G. Chen, "Modification of the surface electronic and chemical properties of Pt(111) by subsurface 3d transition metals," *J. Chem. Phys.* **120**, 10240–10246 (2004).
- ¹³V. Stamenkovic, B. S. Mun, K. J. Mayrhofer, P. N. Ross, N. M. Markovic, J. Rossmeisl, J. Greeley, and J. K. Nørskov, "Changing the activity of electrocatalysts for oxygen reduction by tuning the surface electronic structure," *Angew. Chem., Int. Ed.* **45**, 2897–2901 (2006).
- ¹⁴V. R. Stamenkovic, B. Fowler, B. S. Mun, G. Wang, P. N. Ross, C. A. Lucas, and N. M. Marković, "Improved oxygen reduction activity on Pt₃Ni(111) via increased surface site availability," *Science* **315**, 493–497 (2007).
- ¹⁵P. Strasser, S. Koh, T. Anniyev, J. Greeley, K. More, C. Yu, Z. Liu, S. Kaya, D. Nordlund, H. Ogasawara, M. F. Toney, and A. Nilsson, "Lattice-strain control of the activity in dealloyed core-shell fuel cell catalysts," *Nat. Chem.* **2**, 454–460 (2010).
- ¹⁶T. A. Maark and A. A. Peterson, "Understanding strain and ligand effects in hydrogen evolution over Pd(111) surfaces," *J. Phys. Chem. C* **118**, 4275–4281 (2014).
- ¹⁷L. Zhang, R. Iyyamperumal, D. F. Yancey, R. M. Crooks, and G. Henkelman, "Design of Pt-shell nanoparticles with alloy cores for the oxygen reduction reaction," *ACS Nano* **7**, 9168–9172 (2013).
- ¹⁸X. Zhang and G. Lu, "Computational design of core/shell nanoparticles for oxygen reduction reactions," *J. Phys. Chem. Lett.* **5**, 292–297 (2014).
- ¹⁹B. B. Xiao, X. B. Jiang, and Q. Jiang, "Density functional theory study of oxygen reduction reaction on Pt/Pd₃Al(111) alloy electrocatalyst," *Phys. Chem. Chem. Phys.* **18**, 14234–14243 (2016).
- ²⁰V. Viswanathan, H. A. Hansen, J. Rossmeisl, and J. K. Nørskov, "Universality in oxygen reduction electrocatalysis on metal surfaces," *ACS Catal.* **2**, 1654–1660 (2012).
- ²¹B. Hammer and J. Nørskov, "Electronic factors determining the reactivity of metal surfaces," *Surf. Sci.* **343**, 211–220 (1995).
- ²²V. R. Stamenkovic, B. S. Mun, M. Arenz, K. J. J. Mayrhofer, C. A. Lucas, G. Wang, P. N. Ross, and N. M. Markovic, "Trends in electrocatalysis on extended and nanoscale Pt-bimetallic alloy surfaces," *Nat. Mater.* **6**, 241–247 (2007).
- ²³Y. Ma and P. B. Balbuena, "Role of iridium in Pt-based alloy catalysts for the ORR: Surface adsorption and stabilization studies," *J. Electrochem. Soc.* **157**, B959 (2010).
- ²⁴S. Kattel and G. Wang, "Beneficial compressive strain for oxygen reduction reaction on Pt(111) surface," *J. Chem. Phys.* **141**, 124713 (2014).
- ²⁵R. Srivastava, P. Mani, N. Hahn, and P. Strasser, "Efficient oxygen reduction fuel cell electrocatalysis on voltammetrically dealloyed Pt–Cu–Co nanoparticles," *Angew. Chem., Int. Ed.* **46**, 8988–8991 (2007).
- ²⁶P. Strasser, S. Koh, and J. Greeley, "Voltammetric surface dealloying of Pt bimetallic nanoparticles: An experimental and DFT computational analysis," *Phys. Chem. Chem. Phys.* **10**, 3670 (2008).
- ²⁷M. Escudero-Escribano, P. Malacrida, M. H. Hansen, U. G. Vej-Hansen, A. Velázquez-Palenzuela, V. Tripkovic, J. Schiøtz, J. Rossmeisl, I. E. L. Stephens, and I. Chorkendorff, "Tuning the activity of Pt alloy electrocatalysts by means of the lanthanide contraction," *Science* **352**, 73–76 (2016).
- ²⁸J. Li, Z. Xi, Y. T. Pan, J. S. Spendelow, P. N. Duchesne, D. Su, Q. Li, C. Yu, Z. Yin, B. Shen, Y. S. Kim, P. Zhang, and S. Sun, "Fe stabilization by intermetallic L₁–FePt and Pt catalysis enhancement in L₁–FePt/Pt nanoparticles for efficient oxygen reduction reaction in fuel cells," *J. Am. Chem. Soc.* **140**, 2926–2932 (2018).
- ²⁹A. Khorshidi, J. Violet, J. Hashemi, and A. A. Peterson, "How strain can break the scaling relations of catalysis," *Nat. Catal.* **1**(4), 263–268 (2018).
- ³⁰J. J. Mortensen, L. B. Hansen, and K. W. Jacobsen, "Real-space grid implementation of the projector augmented wave method," *Phys. Rev. B* **71**, 035109 (2005).
- ³¹J. Enkovaara, C. Rostgaard, J. J. Mortensen, J. Chen, M. Dulak, L. Ferrihi, J. Gavnholt, C. Glinsvad, V. Haikola, H. A. Hansen, H. H. Kristoffersen,

- M. Kuisma, A. H. Larsen, L. Lehtovaara, M. Ljungberg, O. Lopez-Acevedo, P. G. Moses, J. Ojanen, T. Olsen, V. Petzold, N. A. Romero, J. Stausholm-Møller, M. Strange, G. A. Tritsaris, M. Vanin, M. Walter, B. Hammer, H. Häkkinen, G. K. H. Madsen, R. M. Nieminen, J. K. Nørskov, M. Puska, T. T. Rantala, J. Schiøtz, K. S. Thygesen, and K. W. Jacobsen, "Electronic structure calculations with GPAW: A real-space implementation of the projector augmented-wave method," *J. Phys.: Condens. Matter* **22**, 253202 (2010).
- ³²A. H. Larsen, J. J. Mortensen, J. Blomqvist, I. E. Castelli, R. Christensen, M. Dułak, J. Friis, M. N. Groves, B. Hammer, C. Hargus, E. D. Hermes, P. C. Jennings, P. Bjerre Jensen, J. Kermode, J. R. Kitchin, E. Leonhard Kolsbjerg, J. Kubal, K. Kaasbjerg, S. Lysgaard, J. Bergmann Maronsson, T. Maxson, T. Olsen, L. Pastewka, A. Peterson, C. Rostgaard, J. Schiøtz, O. Schütt, M. Strange, K. S. Thygesen, T. Vegge, L. Vilhelmsen, M. Walter, Z. Zeng, and K. W. Jacobsen, "The atomic simulation environment—A Python library for working with atoms," *J. Phys.: Condens. Matter* **29**, 273002 (2017).
- ³³B. Hammer, L. B. Hansen, and J. K. Nørskov, "Improved adsorption energetics within density-functional theory using revised Perdew-Burke-Ernzerhof functionals," *Phys. Rev. B* **59**, 7413–7421 (1999).
- ³⁴P. Haas, F. Tran, and P. Blaha, "Calculation of the lattice constant of solids with semilocal functionals," *Phys. Rev. B* **79**, 085104 (2009).
- ³⁵S. Kang, S. Shi, Z. Jia, G. B. Thompson, D. E. Nikles, J. W. Harrell, D. Li, N. Poudyal, V. Nandwana, and J. P. Liu, "Microstructures and magnetic alignment of L_{10} FePt nanoparticles," *J. Appl. Phys.* **101**(9), 09J113 (2007).
- ³⁶G. S. Karlberg, J. Rossmeisl, and J. K. Nørskov, "Estimations of electric field effects on the oxygen reduction reaction based on the density functional theory," *Phys. Chem. Chem. Phys.* **9**, 5158 (2007).
- ³⁷V. Viswanathan, H. A. Hansen, J. Rossmeisl, and J. K. Nørskov, "Unifying the 2e^- and 4e^- reduction of oxygen on metal surfaces," *J. Phys. Chem. Lett.* **3**, 2948–2951 (2012).
- ³⁸V. A. Sethuraman, D. Vairavapandian, M. C. Lafouresse, T. A. Maark, N. Karan, S. Sun, U. Bertocci, A. A. Peterson, G. R. Stafford, and P. R. Guduru, "Role of elastic strain on electrocatalysis of oxygen reduction reaction on Pt," *J. Phys. Chem. C* **119**, 19042–19052 (2015).
- ³⁹H. A. Hansen, V. Viswanathan, and J. K. Nørskov, "Unifying kinetic and thermodynamic analysis of 2e^- and 4e^- reduction of oxygen on metal surfaces," *J. Phys. Chem. C* **118**, 6706–6718 (2014).